Journal of Materials Chemistry

PAPER

Vertically aligned In$_2$O$_3$ nanorods on FTO substrates for photoelectrochemical applications†

Jiayong Gan,[a] Xihong Lu,[a] Teng Zhai,[a] Yufeng Zhao,[a] Shilei Xie,[a] Yanchao Mao,[a] Yueli Zhang,[b] Yangyi Yang*[a] and Yexiang Tong*[a]

Vertically aligned In$_2$O$_3$ nanorod arrays (NRAs) were obtained by annealing the as-prepared In(OH)$_3$ precursors that grew directly on FTO substrates *via* a simple template-free electrochemical assembly process. The absorption edges of In$_2$O$_3$ NRAs show a red-shift to the visible region, and a remarkable photocurrent response under visible light illumination ($\lambda \geq 390$ nm) in photoelectrochemical cells.

Introduction

Because of a decline in the availability of fossil fuels such as oil and coal, increasing energy demands and limited supply may come into conflict in the future, leading the world towards a global energy crisis. Meanwhile, the extensive use of fossil fuels will result in a series of environmental problems. As an environmentally clean alternative energy resource, solar energy has received great interest for environmental pollution and energy crisis considerations in the recent years.[1–3] While progress has been made in several areas of utilizing renewable energy, it is clear that the underexploited potential of solar energy, and especially its application in hydrogen production, represents a potentially limitless source. Since the innovative report published in 1972 for photoelectrochemical water splitting using titanium dioxide (TiO$_2$) photoelectrodes,[4] many studies have been dedicated to developing new materials for photoelectrochemical hydrogen production. Compared to other materials, semiconductor nanomaterials are the most promising candidate for photoelectrochemical (PEC) cells due to their large surface area and size dependent properties, such as increased photon absorption, enhanced charge separation and migration, and surface reactions. Currently, of particular concern is one-dimensional (1D) nanostructures including nanorods, nanowires, and nanobelts because they can provide a direct path for photogenerated charges with reduced grain boundaries and superior charge transport properties.[5]

Transition-metal oxides nanostructures, with their low cost and being easy to obtain, represent a new class of photoelectrode materials that hold great promise for PEC application.[6–11] Impressive results have been obtained recently with TiO$_2$, ZnO, SnO$_2$, NiO and other transition metal oxides for photovoltaic devices.[12–15]

Indium compounds, such as indium hydroxide (In(OH)$_3$) and indium oxide (In$_2$O$_3$), have been investigated intensively for many years because of their novel optical and electrical properties and potential applications in various fields.[16–22] Indium hydroxide is an important semiconductor with a wide band gap ($E_g = 5.15$ eV) and has promising applications as a photocatalyst.[16] Indium oxide is an important transparent conductive oxide (TCO) with a wide band gap (3.65 eV), and is also an important n-type semiconductor. In recent years, considerable efforts have been devoted to the possible applications of In$_2$O$_3$ nanostructures for ultraviolet-visible (UV-vis) lasers, detectors, holographic recorders, thin film transistors, organic light-emitting diodes and gas sensors.[17–22] However, much less notice has been taken of indium oxide as a photovoltaic material owing to its large optical energy band gaps. In fact, In$_2$O$_3$ fulfils some important requirements for the direct photoelectrolysis of water in that the position of the conduction and valence band edges bracket the redox potentials of water, and In$_2$O$_3$ has an excellent conductivity and stability.[23] Nevertheless, its large band gap that makes it transparent to visible light and decreases its potential efficiency for water splitting under solar illumination still remains a problem. It is known that the properties of nanomaterials depend strongly on the morphology and size.[24] Thus, the synthesis of In$_2$O$_3$ nanostructures with controllable morphology and properties is of particular significance.

Various methods such as chemical vapor deposition, hot-injection techniques, organic solution synthetic routes, hydrothermal methods, and solvothermal methods have been exploited to synthesize indium hydroxide and indium oxide with various

aKLGHEI of Environment and Energy Chemistry, MOE Laboratory of Bioinorganic and Synthetic Chemistry, School of Chemistry and Chemical Engineering, Institute of Optoelectronic and Functional Composite Materials, Sun Yat-sen University, Guangzhou, 510275, P. R. China. E-mail: chedhx@mail.sysu.edu.cn; cesyyy@mail.sysu.edu.cn; Fax: +86 20 84112245; Tel: +86 20 84110071

bSchool of Physics and Engineering, Sun Yat-Sen University, Guangzhou, 510275, P. R. China

† Electronic supplementary information (ESI) available: details of the growing mechanism of In(OH)$_3$ nanostructures: SEM images, schematic representation of the formation process of precursor In(OH)$_3$ nanosheets, nanocubes and NRAs. See DOI: 10.1039/c1jm11774b

This journal is © The Royal Society of Chemistry 2011

J. Mater. Chem., 2011, **21**, 14685–14692 | 14685

morphologies.[25–29] Among these methods, electrochemical deposition is a promising method for large-scale fabrication of the nanomaterials, owing to its simplicity, low cost, ease of scale-up, and environmental friendliness,[30,31] but the investigations by this technique on In_2O_3 nanorod arrays (NRAs) have been quite limited. Herein, we report an approach for the synthesis of In_2O_3 NRAs based on a template- and surfactant-free electrochemical deposition method from aqueous solution. By adjusting the reaction parameters, various morphologies of the In_2O_3 nanostructures including NRAs can be readily obtained. A remarkable red shift to the visible region at the absorption edges of these In_2O_3 NRAs is also clearly observed. Furthermore, under visible light illumination ($\lambda \geq 390$ nm), the NRAs exhibit an evident photovoltaic response. This present work aims at providing a new approach for large-scale, low-cost, controllable electrochemical growth of vertically-aligned NRAs on all kinds of conductive substrates. Also it presents a new opportunity in constructing electronic and various heterostructure-photoelectronic devices based on In_2O_3 NRAs.

Experimental section

Synthesis of In_2O_3 NRAs

The analytical grade $In(NO_3)_3\cdot3H_2O$ and NH_4Cl were commercially purchased from Sinopharm Chemical Reagent Co., Ltd., China. Electrodeposition of $In(OH)_3$ nanorods was performed in a conventional three-electrode cell using a home-made HDV-7C potentiostatic apparatus with a graphite rod counter electrode and a saturated Ag/AgCl reference electrode, which was connected to the cell with a double salt bridge. The working electrode was an F-doped SnO_2-coated glass (FTO) with a sheet resistance of 14 $\Omega/\square$. The FTO glass was cleaned ultrasonically in distilled water, ethanol, and acetone and then rinsed in distilled water again before electrodeposition. The electrolytic solution contained 0.02 M $In(NO_3)_3$ and 0.1 M NH_4Cl, and the reaction temperature was kept at 90 °C. After deposition, the film was washed by water and dried in air at 25 °C for 10 h. In_2O_3 could be obtained via a thermal decomposition method using the as-prepared films in air at 400 °C for 2 h.

Characterizations

The surface morphology and composition of the samples were analyzed by scanning electron microscope (SEM, Quanta 400). The structures of the samples were investigated via X-ray diffraction (XRD, Bruker, D8 ADVANCE) with Kα radiation ($\lambda = 1.5418$ Å) and transmission electron microscopy (TEM, 200 kV, JEM2010-HR). X-Ray photoelectron spectroscopy (XPS, ESCALAB250) was used to assess the chemical state and surface composition of the deposits. The optical properties of the products were measured with a UV-vis-NIR spectrophotometer (UV, Shimadzu UV-2450) and a combined fluorescence lifetime and steady state spectrometer (PL, EDINBURGH). The In_2O_3 measurements of SEM, XPS, XRD and UV-spectra were directly carried out on the samples without removing the substrates.

PEC measurements were carried out in a three-electrode cell with a flat quartz window to facilitate illumination of the photoelectrode surface. The working electrode is the In_2O_3 film, while a graphite rod and a saturated Ag/AgCl electrode were used as counter and reference electrodes, respectively. A 1 M CH_3OH aqueous solution was used as the electrolyte. And the pH value was adjusted to 12 by NaOH. A 500 W Xe arc lamp directed at the quartz photoelectrochemical cell was applied as the illumination source. A UV filter (absorbance $\lambda \leq 390$ nm) was used to cut off the UV energy. A 0.16 cm^2 region (0.4 cm $\times$ 0.4 cm) of the photoelectrode surface was illuminated with intermittent light irradiation. A CHI 750a electrochemical workstation (Chenhua, Shanghai) was used to record the photocurrent densities by using the difference between the light-off (dark current) and light-on currents acquired consecutively.

Results and discussion

1. Film deposition and materials characterization

The XRD pattern was used to examine the crystalline phase of the as-prepared NRA samples, and the result of the $In(OH)_3$ NRAs prepared via cathodic electrodeposition in 0.02 M $In(NO_3)_3$ + 0.1 M NH_4Cl with a current density of 1 mA cm^{-2} for 60 min at 90 °C is presented in Fig. 1. All of the reflections of the XRD pattern could be indexed to body-centered cubic $In(OH)_3$ with a lattice constant $a = 7.96$ Å, compatible with JCPDS Card No. 16-0161. No peaks of impurities were observed, indicating that the final product is a pure phase compound. The narrow and strong peaks showed good crystallinity of $In(OH)_3$ NRAs. Fig. 1b shows that pure phase In_2O_3 can be obtained by calcination of the as-made $In(OH)_3$. All of the peaks can be indexed to a pure cubic phase [space group: $Ia3$] of In_2O_3 with a lattice constant of $a = 10.02$ Å, which is very consistent with JCPDS Card No. 65-3170.

Fig. 2a and 2b show the scanning electron microscopy (SEM) images of the as prepared $In(OH)_3$ NRAs. Large scale arrays of the well aligned $In(OH)_3$ rods were successfully grown on the FTO substrates (see Fig. 2a). And some of the $In(OH)_3$ nanorods aggregated into flower-like bundles that grew on the top of the NRAs. The high magnification SEM image (inset in Fig. 2a) indicates that the diameter of a nanorod is about 300 nm and the top of the rod is smooth. The cross-sectional SEM image of the
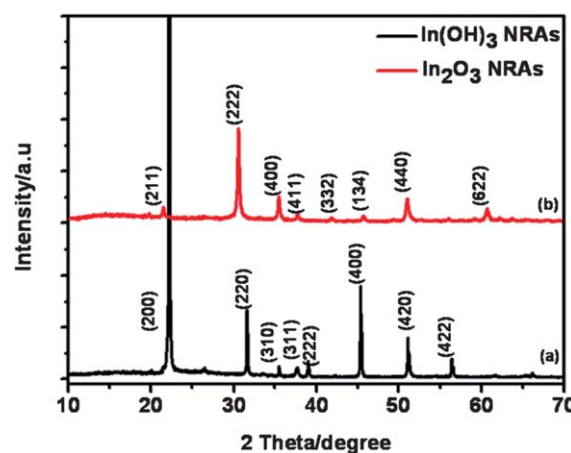
Fig. 1 Comparison of XRD patterns of as-prepared (a) $In(OH)_3$ NRAs and (b) In_2O_3 NRAs obtained by calcination in air at 400 °C, respectively.
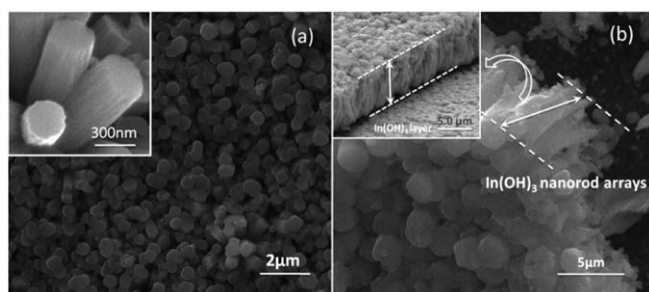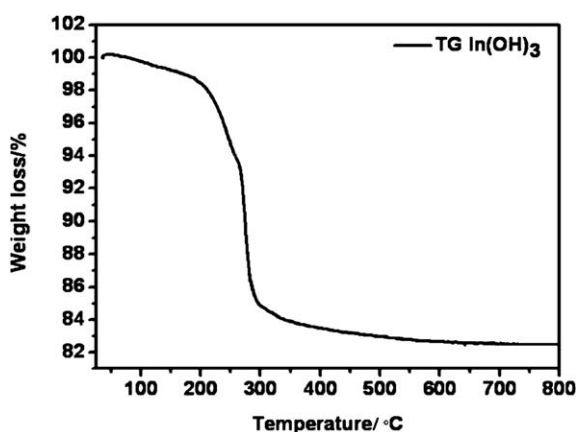
Fig. 2 SEM images of the as-synthesized In(OH)₃ NRAs on FTO substrates.

In(OH)$_3$ NRAs is given in Fig. 2b, showing that ordered nanorods of about 5.0 μm in length grew vertically from the substrate.

TG analysis has been taken to study the phase transformation of the sample. The thermal behavior of In(OH)$_3$ dehydrated to In$_2$O$_3$ was investigated in the temperature range of 25–800 °C. Fig. 3 shows the TG curves of the as prepared In(OH)$_3$ NRAs. It can be seen that the dominant mass loss in the range of 150–400 °C is 16%, which can be attributed to conversion from In(OH)$_3$ to In$_2$O$_3$, in good agreement with a theoretical weight loss (16.3%). The gradual mass loss from room temperature to 150 °C may be due to evaporation of the adsorbed water species on In(OH)$_3$ surfaces. The main mass loss variation was observed at 276 °C.

On the basis of the TG results above, we believe that In$_2$O$_3$ NRAs could be obtained by calcination of as-prepared In(OH)$_3$ NRAs over 400 °C. Fig. 4 shows the morphology of In$_2$O$_3$ nanostructures obtained from In(OH)$_3$ annealed at 400 °C for 2 h. The initial shape and size of the nanorods were basically kept the same as the precursors In(OH)$_3$. Closer observation (inset in Fig. 4b) reveals that there are cracks on the surface of the NRAs, which may be attributed to the removal of –OH (dehydration) during the calcination process. The result indicates that In$_2$O$_3$ NRAs were successfully obtained with the morphologies well-inherited from In(OH)$_3$ NRAs. In order to understand the chemical composition of the calcined product, X-ray photoelectron spectroscopy (XPS) analysis was performed on the In$_2$O$_3$ NRAs. Fig. 4c displays the In 3d core level spectrum of the In$_2$O$_3$ NRAs. Two peaks located at 444.6 and
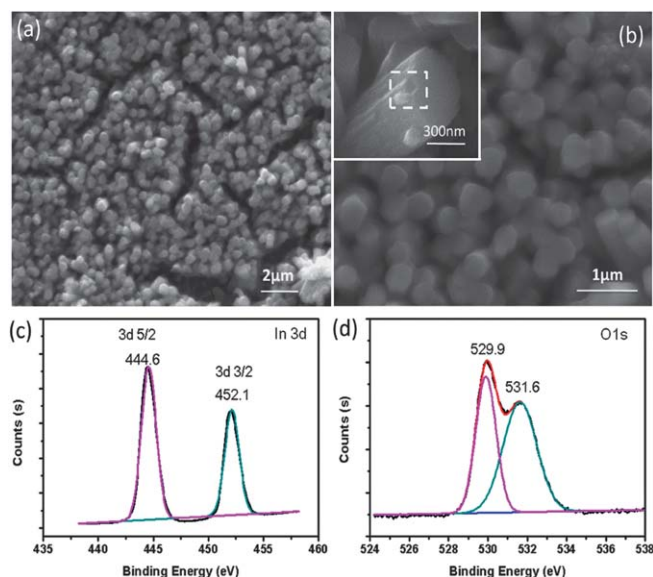
**Fig. 4** (a,b) SEM images of In$_2$O$_3$ NRAs obtained by calcination of as-prepared In(OH)$_3$ NRAs in air at 400 °C for 2 h; (c) In 3d XPS spectrum of the In$_2$O$_3$ NRAs; (d) O 1s XPS spectrum of the In$_2$O$_3$ NRAs.

452.1 eV are clearly observed, which can be attributed to the characteristic spin–orbit split 3d 5/2 and 3d 3/2, respectively.[29] This result indicates the In valency is mainly +3 in the product. Fig. 4d is the O 1s core level spectrum, clearly showing that two peaks can be identified. The peak at about 529.9 eV originates from the oxygen bond of In–O–In, and the peak at 531.6 eV corresponds to the surface oxygen defects.[29] Thus, the XPS results demonstrated that the calcined product is In$_2$O$_3$ with some oxygen defects.

The crystal structure of In$_2$O$_3$ nanorods was investigated by TEM. A low-magnification TEM image of part of an individual nanorod with column-rodlike structure is illustrated in Fig. 5a. The high-resolution TEM (HRTEM) image (Fig. 5b) of the selected area marked in Fig. 5a reveals the lattice fringe spacing of 0.419 and 0.290 nm (see the magnified HRTEM in Fig. 5f),

Fig. 3 TG curves of the as-prepared In(OH)₃ NRAs.
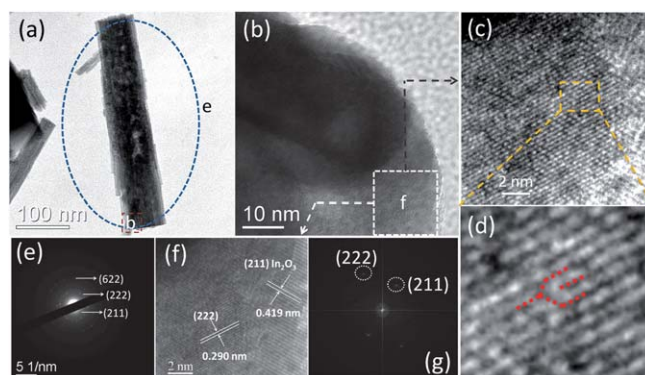
Fig. 5 (a) TEM image; (b) HRTEM image; (c) the corresponding Fourier filtered image of the selected part marked in (b); (d) enlarged image of the dashed rectangle marked in (c); (e) SAED pattern of the area marked in the TEM image of (a); (f) enlarged image of the selected part marked in (b); (g) FFT pattern that transferred from the HRTEM image of (f); of the In₂O₃ NRAs on FTO substrates.

which matches well with the (211) and (222) lattice spacing of body-centered-cubic (bcc) In_2O_3. Fig. 5g is the fast Fourier transmission (FFT) pattern of Fig. 5f. The diffraction spots in this FFT pattern can be indexed to the (222) and (211) plane, which is in accord with the results in Fig. 5f. Fig. 5e is the corresponding SAED pattern of this rod (marked by a dashed ellipse in Fig. 5a), confirming that the polycrystalline structure of a nanorod was formed after annealing. Fig. 5c displays the FFT image of the rod (marked by the dashed square in Fig. 5b), which exhibits some misfit dislocations. This indicates the presence of defects in the In_2O_3 nanorod, which are related with the interesting optical properties of the NRAs.
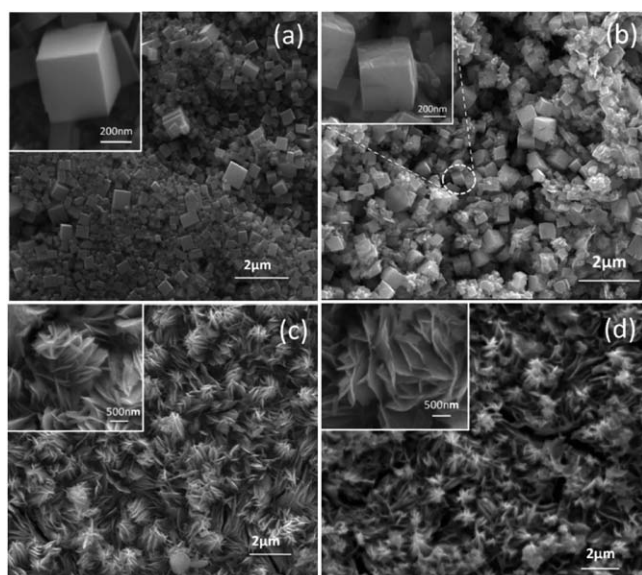
2. Morphology adjusting

Fig. 6 shows the SEM images of $In(OH)_3$/In_2O_3 nanocubes and nanosheets, which are obtained *via* simply adjusting the reaction conditions. $In(OH)_3$ nanocubes with a size of ~400 nm (Fig. 6a) are synthesized at low In^{3+} concentrations ($[In^{3+}] = 0.008$ M) at 70 °C with a potential of −1.2 V (*vs.* Ag/AgCl) for 120 min. The surfaces of the nanocubes are smooth, and the angle between the adjacent edges is relatively close to 90°, indicating that their cubic shape is quite regular. The cube is simply enclosed with crystal faces of {001} surfaces,[32] which can be found in the enlarged SEM image (Fig. 6a inset). As to the sample deposited at a potential of −1.2 V (*vs.* Ag/AgCl), from 0.008 M $In(NO_3)_3$ solution at 70 °C for 60 min, $In(OH)_3$ nanosheets with a side length approximately between 600 and 700 nm can be found, which is shown in Fig. 6c. Some of them accumulated into flower-like units on a large scale. After calcination, In_2O_3 nanocubes and nanosheets basically inherited their parents' morphology, as shown in Fig. 6b and 6d, Thus, the morphology of $In(OH)_3$ and In_2O_3 can be readily shape-controlled by adjusting the reaction conditions. In order to understand the growth mechanism of these morphologies, the formation process of $In(OH)_3$ nanostructures was studied by the controlled
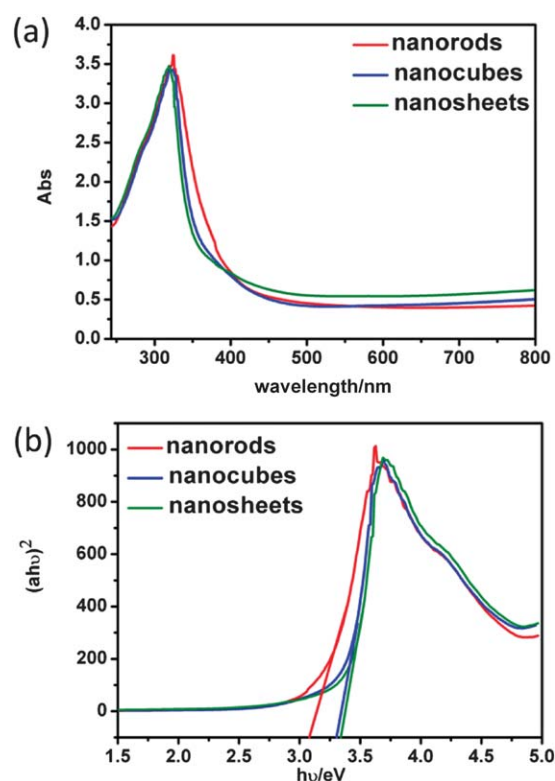
experiments with different deposition times, as shown in Fig. S1–3† and discussed in the supporting information. It is believed that the growth of NRAs can be attributed to a seed-layer based electrochemical growth mechanism while the formation of other nanostructures adopted a different route.

3. Optical properties and photoelectrochemical application

The UV-vis absorption spectra of In_2O_3 NRAs, nanocubes and nanosheets are shown in Fig. 7a. It is observed that the absorption band of In_2O_3 NRAs is red-shifted (~8 nm) compared to nanocubes and nanosheets, which indicates that these NRAs maybe have a better performance for utilizing the visible light. The direct optical band gap (E_g) of a semiconductor nanomaterial can be calculated from the equation of $(\alpha h\nu)^2 = A (h\nu - E_g)$, where $h\nu$ is the photon energy, α is the absorption coefficient, and A is a constant for the material.[33] As shown in Fig. 7b, the calculated direct E_g for the three samples is about 3.09, 3.29, and 3.32 eV, respectively. These values are relatively smaller than the theoretical value of bulk In_2O_3. In the last few years, there have been two types of theories proposed for explaining the red-shift phenomenon of the optical band gap of In_2O_3 nanostructures. The first is the shape effect. It is known that if the particle size reduces to a certain scale, the optical band gap will be blue-shifted due to the quantum confinement effect.[34] For instance, a red-shift phenomenon of the CeO_2 nanoneedles was observed by Chang's group, and they considered that the shape effect is responsible for this result.[35] The other is the presence of defects, which is generally accepted for the

Fig. 7   (a) UV-visible absorption spectra and (b) $(\alpha h\nu)^2$ *vs.* $h\nu$ curves for these In_2O_3 nanostructures.

**Fig. 6**   SEM images of different morphologies of the samples (a,c) before and (b,d) after calcination at 400 °C.

explanation with the red-shift of the nanostructures. For examples, Patsalas et al.[36,37] have found that the red-shift of the optical band gap of a CeO_2 film is correlated with the increase of the defect content. In our case, the size of the In_2O_3 nanorods, nanosheets and nanocubes is larger than 100 nm. Furthermore, the XPS results (discussed above) have demonstrated that the In_2O_3 NRAs have large numbers of oxygen defects. In addition, the PL emissions at ~410 nm (discussed at the next paragraph) also confirm the presence of oxygen defects in the samples. Similar to other oxide semiconductors, the oxygen vacancies would induce the formation of new energy levels in the band gap. Therefore, in view of the discussion above, we believe that the red-shift of the absorption edge is attributed to shape effect and the surface defects.

For better understanding of the presence of defects in the samples, the room temperature photoluminescence (PL) spectra of samples were studied using a combined fluorescence lifetime and steady state spectrometer (EDINBURGH).

As shown in Fig. 8a and 8b, it is evident that strong emission bands were observed, at ~410 nm for the In_2O_3, and at ~380 nm for the $In(OH)_3$ nanocubes and NRAs, respectively. In general, bulk In_2O_3 does not emit light,[38] while its nanostructures can emit visible and UV light. Our experiment also showed that the commercial bulk In_2O_3 power emitted no detectable light. This may be because the bulk In_2O_3 material lacks of defects. PL emission by nanoparticles in the visible range was mainly attributed to the presence of oxygen vacancies and the emission peaks are commonly referred to as deep level or trap state emissions due to oxygen vacancies.[39–41] Generally speaking, emission spectra can be divided into two broad categories: the near-band-edge (NBE) emissions and deep-level (DL) emissions. As for $In(OH)_3$ without annealing process, detectable UV emission at ~380 nm (see Fig. 8a) is observed. The results indicate that they possess a number of impurities and structure defects, such as indium vacancies. This leads to a high NBE-emissions-to-DL-emissions ratio, which results in detectable UV emission at room temperature.[42,43] It is obvious that strong emission bands at ~410 nm were observed for the two samples of In_2O_3 after 400 °C calcination (see Fig. 8b). This indicates the existence of surface oxygen vacancies and defects of In_2O_3 nanoparticles. Hence, based on the PL results above, we believed the presence of defects arising from the oxygen deficiencies in In_2O_3 still remained or even increased after the annealing process. Also, the relative intensity of the emission band in In_2O_3 NRAs is stronger than that for In_2O_3 nanocubes, which clearly shows that the In_2O_3 NRAs possess higher oxygen vacancies. Similarly, $In(OH)_3$ NRAs have more defects than nanocubes alike.

Well-aligned NRAs with a narrow band gap are very promising candidates for photovoltaic applications. The as-prepared In_2O_3 NRAs are expected to be used as photoelectrodes. The photoelectrochemical properties of In_2O_3 NRAs electrodes were characterized by measuring the photocurrent at zero bias under visible light illumination ($\lambda \geq 390$ nm). The photocurrent response of the photoanodes prepared from the three kinds of In_2O_3 nanostructures when the light source was switched on and off was shown in Fig. 9. Obviously, all the samples exhibit an n-type semiconductor feature photovoltaic response under visible light illumination. The In_2O_3 NRAs electrode exhibited the most remarkable photoelectrochemical response: over 2 times higher than the nanocubes and nanosheets electrodes, at approximately 2.0 μA cm^{-2} when exposed to light. Of note is that the response time to both the on and the off cycles was $\leq$500 ms, indicating that it is not a gradual response but a very quick and well-defined increase. Also, once exposed to light, the current appears to be constant. The enhancement of photocurrent for NRAs can be attributed to the improvement of light-harvesting, as shown in Fig. 7a.
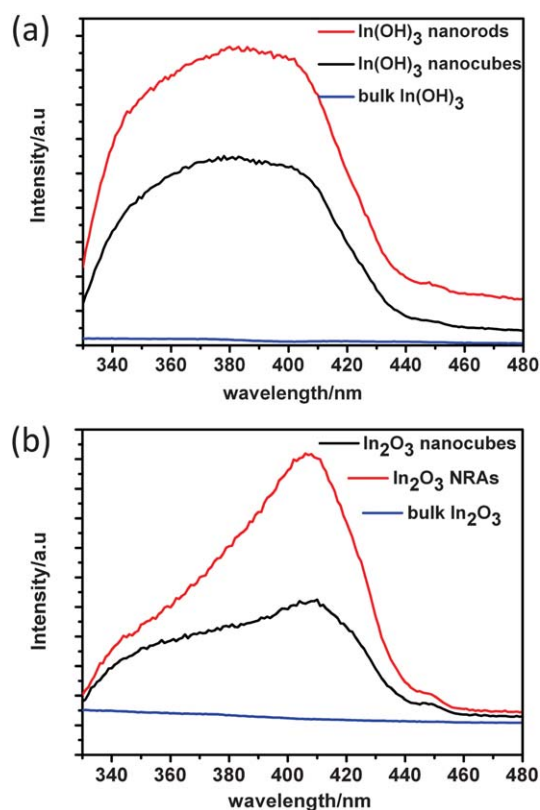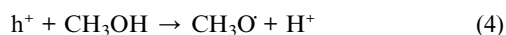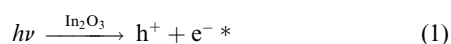

Fig. 8 Room temperature photoluminescence spectra of (a) $In(OH)_3$ nanocubes, NRAs and bulk $In(OH)_3$; (b) In_2O_3 nanocubes, NRAs and bulk In_2O_3 with the excitation wavelength of 288 nm.
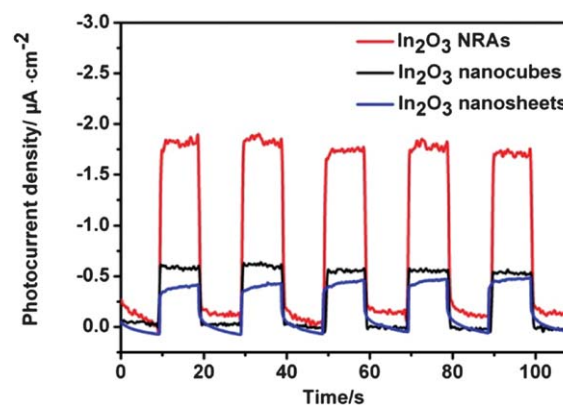
Fig. 9 Photocurrent response of the photoanodes prepared from In_2O_3 with different morphologies to light on–off under visible light illumination ($\lambda \geq 390$ nm).

As is known to all, both the capacity of light-harvesting and the separation of electron–hole pairs are key factors determining the photoelectrochemical activity.[44,45] Under the illumination of light with incident photon energies larger than the E_g, the photoelectrons in semi-conductive materials would be excited from the valance band to the conducting band and a photocurrent is generated. The electron–hole pairs will recombine unless they are separated quickly, which is responsible for the low photon conversion efficiency. The schematic diagram of the In$_2$O$_3$ NRAs photoelectrochemical cell is presented in Fig. 10.

In our case, oxygen vacancies in NRAs may induce the formation of new energy levels in the band gap. The electrons are first produced in the new energy levels of In$_2$O$_3$ with less photon energy, and then transit to the conducting band under sustained visible light illumination. The corresponding holes are present in the valence band. Then the photogenerated electrons move to the counter electrode for the reduction of water, while the holes move to the semiconductor/electrolyte interface for the oxidation of methanol. The photoelectrochemical reactions are proposed as follows:[46]

$$h\nu \xrightarrow{\text{In}_2\text{O}_3} h^+ + e^- * \qquad (1)$$

$$e^- * \rightarrow e^- \qquad (2)$$

$$e^- + 2H^+ \rightarrow H_2 \qquad (3)$$

$$h^+ + CH_3OH \rightarrow CH_3O^\cdot + H^+ \qquad (4)$$

By comparison, the main difficulty for photovoltaic application of bulk In$_2$O$_3$ is its wide band gap of 3.65 eV, forbidding the separation of photoelectrons and holes. It is believed that the higher photocurrent responses of NRAs are related to the red-shift of the optical band gap. Additionally, the red-shift phenomenon is associated with different energy levels caused by oxygen vacancies. So, it is able to use less energy to activate the photoelectrons. Here, the In$_2$O$_3$ samples were prepared from In

(OH)$_3$ precursors after annealing at 400 °C, and the vacancies invariably exist or even increased. On the one hand, vertically-oriented In$_2$O$_3$ NRAs with a high surface-to-volume ratio may be beneficial for the formation of quantities of oxygen vacancies. On the other hand, these NRAs can provide a high interfacial area, high active surface area and superior electrical pathways for the transport of electrons as well. Thus, the rate of hole–electron recombination will be reduced, which effectively improves the carrier separation efficiency. The photogenerated holes transfer to the surface of In$_2$O$_3$ rather than undergoing bulk recombination, and then would be effectively scavenged by CH$_3$OH, and as a result it enhances the photo-electrochemical behaviors directly.

In recent years, less notice has been taken of In$_2$O$_3$ as a photovoltaic material owing to its large optical energy band gap. If the light illumination over 390 nm or over 420 nm in our PEC experiment used bulk In$_2$O$_3$ as the photoanode, no detectable photocurrent response will be observed (data not shown). By using In$_2$O$_3$ NRAs, though a negligible amount of light above 400 nm is absorbed, an obvious photocurrent up of to several μA cm^{-2} can be collected. This may be inefficient in harvesting solar light. However, our work displayed that vertically oriented In$_2$O$_3$ nanorods (5.0 μm length) with such a wide band gap can provide superior electrical pathways for the transport of electrons, which will be able to improve the efficiency in photovoltaic applications. Thus, the NRAs show a higher photocurrent response, as shown in Fig. 9.

4. Impact factors of PEC performance of In$_2$O$_3$ NRAs

In addition, we studied the effect of the length of the NRAs and electrolyte compositions on the PEC behavior of the materials. Fig. 11a shows the photocurrent response of the photoanodes prepared from the two kinds of In$_2$O$_3$ NRAs. The corresponding SEM images are shown in Fig. 11b and 11c. The length of the as-prepared NRAs is about 5 μm and 3 μm respectively. The 5 μm-In$_2$O$_3$ NRAs electrode exhibited a higher photocurrent density
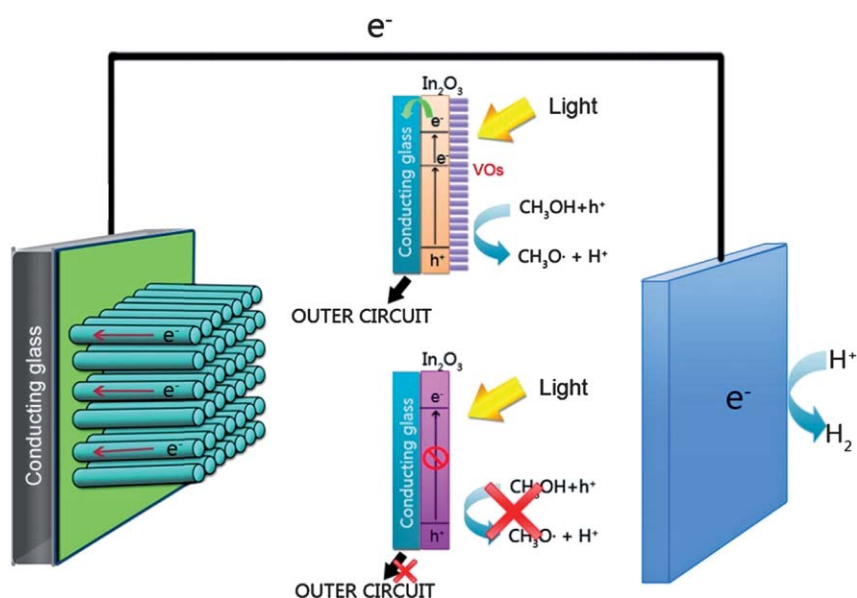

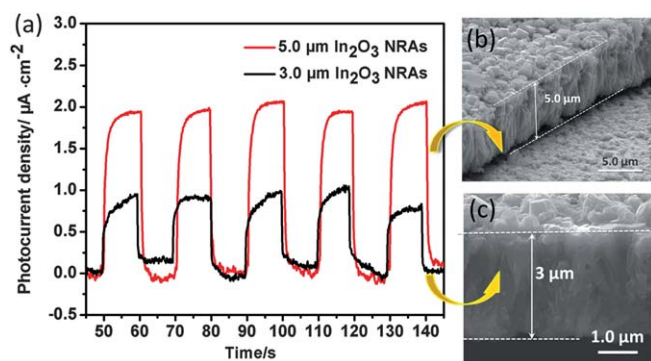**Fig. 10** The schematic diagram and the mechanism of the In$_2$O$_3$ NRAs photoelectrochemical cell.

Fig. 11 (a) Photocurrent response of the photoanodes prepared from In_2O_3 with different lengths to light on–off under visible light illumination ($\lambda \geq 390$ nm); (b,c) the cross-sectional SEM images of the In_2O_3 NRAs with different lengths, 5 μm, 3 μm, respectively.

than the 3 μm-In_2O_3 NRAs. This enhanced photocurrent can be ascribed to the higher specific area of the long NRAs, which may greatly facilitate the diffusion of active species and transport of electrons.[47]

Fig. 12 shows the photocurrent response of the 5.0 μm photoanodes in different electrolyte compositions. 1 M CH_3OH, 1 M Na_2S, 1 M Na_2SO_3 aqueous solutions were used as the electrolyte, respectively. The pH was adjusted to the same value of 12 by NaOH. The photocurrent collected in Na_2S or Na_2SO_3 shows a high response, up to 12.0 μA cm^{-2}. It can be seen that the photocurrent response of In_2O_3 NRAs in the Na_2S system is the best; the second is in Na_2SO_3;and the worst is in CH_3OH. The addition of the Na_2S (Na_2SO_3, CH_3OH) is not only used as the supporting electrolyte, but it also acts as a sacrificial reagent for the consumption of photogenerated holes. This result indicates that the consumption of holes in Na_2S aqueous solution is more efficient than those in Na_2SO_3 and CH_3OH aqueous solution, which might be due to their different redox capability[48] and investigations into the true reason are now in progress. Therefore, based on the results above, it could be concluded that the length of the NRAs and the composition of electrolytes strongly affect PEC performances of the photoanode.
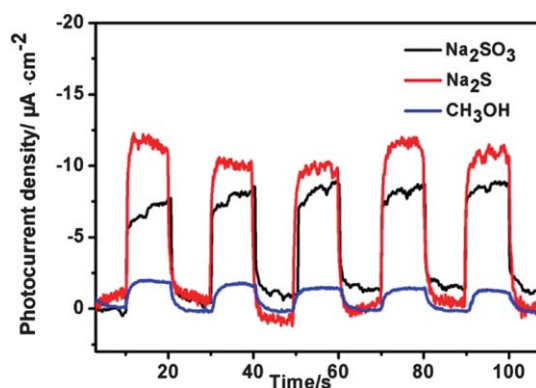
Fig. 12 Photocurrent response of the photoanodes prepared from 5 μm-In_2O_3 with different electrolytes to light on–off under visible light illumination ($\lambda \geq 390$ nm).

Conclusions

In summary, we have reported that various In_2O_3 NRAs could be successfully synthesized on FTO substrates by an electrochemical assembly process without any templates or surfactants. The study shows that the morphology of the final products can be controlled by simply adjusting the reaction time, concentration, potential or current density, which represents a simple, quick and economical method for the preparation and the controllable growth of In_2O_3 nanorods. A red-shift toward the visible region on the absorption edges of the NRAs is clearly observed. They exhibit a photovoltaic response under visible light illumination ($\lambda \geq 390$ nm). In particular, the length of the NRAs and electrolyte compositions strongly affect the PEC efficiencies. The better photoelectrochemical performance demonstrates that the In_2O_3 NRAs are very promising candidates for PEC cells. We also believe that various In_2O_3 nanostructures grown directly on conductive substrates will attract a wide range of attention in catalysis, photodetectors and sensing applications. This study displays a promising template-free electrochemical approach for building In_2O_3 NRAs on conductive substrates, as well as opportunities to assemble all sorts of heterostructure-photoelectrochemical devices based on In_2O_3 NRAs.

Acknowledgements

Notes and references

1 H. Tong, N. Umezawa, J. Ye and T. Ohno, *Energy Environ. Sci.*, 2011, **4**, 1684.
2 M. J. Bierman and S. Jin, *Energy Environ. Sci.*, 2009, **2**, 1050.
3 M. Pagliaro, A. G. Konstandopoulos, R. Ciriminna and G. Palmisano, *Energy Environ. Sci.*, 2010, **3**, 279.
4 A. Fujishima and K. Honda, *Nature*, 1972, **238**, 37.
5 A. I. Hochbaum and P. D. Yang, *Chem. Rev.*, 2010, **110**, 527.
6 R. Asahi, T. Morikawa, T. Ohwaki, K. Aoki and Y. Taga, *Science*, 2001, **293**, 269.
7 O. Khaselev and J. A. Turner, *Science*, 1998, **280**, 425.
8 V. M. Aroutiounian, V. M. Arakelyan and G. E. Shahnazaryan, *Sol. Energy*, 2005, **78**, 581.
9 C. A. Grimes, O. K. Varghese and S. Ranjan, *Light, Water, Hydrogen: The Solar Generation of Hydrogen by Water Photoelectrolysis*, New York, 2008.
10 G. M. Wang, X. Y. Yang, F. Qian, J. Z. Zhang and Y. Li, *Nano Lett.*, 2010, **10**, 1088.
11 R. van de Krol, Y. Q. Liang and J. Schoonman, *J. Mater. Chem.*, 2008, **18**, 2311.
12 Q. F. Zhang, C. S. Dandeneau, X. Y. Zhou and G. Z. Cao, *Adv. Mater.*, 2009, **21**, 4087.
13 P. Qin, M. Linder, T. Brinck, G. Boschloo, A. Hagfeldt and L. C. Sun, *Adv. Mater.*, 2009, **21**, 2993.
14 N. T. Hahn, H. Ye, D. V. Flaherty, A. J. Bard and C. B. Mullins, *ACS Nano*, 2010, **4**, 1977.
15 G. K. Mor, K. Shankar, M. Paulose, O. K. Varghes and C. A. Grimes, *Nano Lett.*, 2006, **6**, 215.
16 S. Avivi, Y. Mastai and A. Gedanken, *Chem. Mater.*, 2000, **12**, 1229.
17 D. Zhang, C. Li, S. Han, X. Liu, T. Tang and W. Jin, *Appl. Phys. A: Mater. Sci. Process.*, 2003, **77**, 163.

This journal is © The Royal Society of Chemistry 2011

J. Mater. Chem., 2011, **21**, 14685–14692 | 14691

18 G. Korotcenkov, V. Brinzari, A. Cerneavschi, M. Ivanov, V. Golovanov and A. Cornet, *Thin Solid Films*, 2004, **460**, 315.
19 S. Maillis, L. Boutsikaris, N. Vainos, C. Xirouhaki, G. Vasiliou and N. Garawal, *Appl. Phys. Lett.*, 1996, **69**, 2459.
20 G. Lavareda, C. Nunes de Carvalho, E. Fortunato, A. Ramos, E. Alves and O. Conde, *J. Non-Cryst. Solids*, 2006, **352**, 2311.
21 C. G. Granquist, *Sol. Energy Mater. Sol. Cells*, 2000, **60**, 2301.
22 K. L. Chopra and S. R. Das, *Thin Film Solar Cell*, Plenum Press, New York, 1983.
23 A. J. Nozik, *Annu. Rev. Phys. Chem.*, 1978, **29**, 189.
24 A. Ghicov and P. Schmuki, *Chem. Commun.*, 2009, 2791.
25 Y. P. Fang, X. G. Wen and S. H. Yang, *Angew. Chem., Int. Ed.*, 2006, **45**, 4655.
26 Z. Q. Liu, D. H. Zhang, S. Han, C. Li, T. Tang, W. Jin, X. L. Liu, B. Lei and C. W. Zhou, *Adv. Mater.*, 2003, **15**, 1754.
27 S. E. Lin and W. C. J. Wei, *J. Am. Ceram. Soc.*, 2006, **89**, 527.
28 C. H. Liang, G. W. Meng, Y. Lei, F. Phillipp and L. D. Zhang, *Adv. Mater.*, 2001, **13**, 1330.
29 B. X. Li, Y. Xie, M. Jing, G. X. Rong, Y. C. Tang and G. Z. Zhang, *Langmuir*, 2006, **22**, 9380.
30 X. H. Lu, D. Z. Zheng, J. Y. Gan, Z. Q. Liu, C. L. Liang, P. Liu and Y. X. Tong, *J. Mater. Chem.*, 2010, **20**, 7118.
31 X. H. Lu, D. Z. Zheng, P. Zhang, P. Liu and Y. X. Tong, *Chem. Commun.*, 2010, **46**, 7721.
32 T. Yan, X. Wang, J. Long, P. Liu, X. Fu, G. Zhang and X. Fu, *J. Colloid Interface Sci.*, 2008, **325**, 425.
33 D. Pradhan and K. T. Leung, *Langmuir*, 2008, **24**, 9707.
34 Z. X. Li, L. L. Li, Q. Yuan, W. Feng, J. Xu, L. D. Sun, W. G. Song and C. H. Yan, *J. Phys. Chem. C*, 2008, **112**, 18405.
35 H. Y. Chen and H. Y. Chang, *Solid State Commun.*, 2005, **133**, 593.
36 P. Patsalas, S. Logothetidis and C. Metaxa, *Appl. Phys. Lett.*, 2002, **81**, 466.
37 P. Patsalas, S. Logothetidis, L. Sygellou and S. Kennou, *Phys. Rev. B: Condens. Matter*, 2003, **68**, 035104.
38 Y. Ohhata, F. Shinoki and S. Yoshida, *Thin Solid Films*, 1979, **59**, 255.
39 M. Mazzera, M. Zha, D. Calestani, A. Zappettini, L. Lazzarini and G. Salviati, *Nanotechnology*, 2007, **18**, 355707.
40 P. Guha, S. Kar and S. Chaudhuri, *Appl. Phys. Lett.*, 2004, **85**, 3851.
41 X. S. Peng, G. W. Meng, J. Zhang, X. F. Wang, Y. W. Wang and C. Z. Wang, *J. Mater. Chem.*, 2002, **12**, 1602.
42 Y. C. Kong, D. P. Yu, B. Zhang, W. Fang and S. Q. Feng, *Appl. Phys. Lett.*, 2001, **78**, 407.
43 D. M. Bagnall, Y. F. Chen, Z. Zhu, T. Yao, S. Koyama, M. Y. Shen and T. Goto, *Appl. Phys. Lett.*, 1998, **73**, 1038.
44 Y. Tak, S. J. Hong, J. S. Lee and K. J. Yong, *J. Mater. Chem.*, 2009, **19**, 5945.
45 J. Zhang, J. H. Bang, C. C. Tang and P. V. Kamat, *ACS Nano*, 2010, **4**, 387.
46 V. Korzhak, N. I. Ermokhina, A. L. Stroyuk, V. K. Bukhtiyarov, A. E. Raevskaya, V. I. Litvin, S. Y. Kuchmiy, V. G. Ilyin and P. A. Manorik, *J. Photochem. Photobiol., A*, 2008, **198**, 126.
47 R. Berank, H. Tsuchiya, T. Sugishima, J. M. Macak, L. Taveira, S. Fujimoto, H. Kisch and P. Schmuki, *Appl. Phys. Lett.*, 2005, **87**, 243114.
48 X. H. Lu, T. Zhai, H. N. Cui, J. Y. Shi, S. L. Xie, Y. Y. Huang, C. L. Liang and Y. X. Tong, *J. Mater. Chem.*, 2011, **21**, 5569.